Accepted Manuscript

Numerical study of bubbles rising and merging during convective boiling in micro-channels

Qingming Liu* and Björn Palm

Department of Energy Technology, Royal Institute of Technology, KTH

Brinellvägen 68, 100 44-SE, Stockholm, Sweden

Research highlights

- Lateral merger of bubbles is observed during flow boiling in micro channels.
- A three dimension numerical study on this process has been done by CLSVOF method.
- The whole process has three sub-stages: sliding, merger, and post-merger.
- The evaporation rate is much higher in the first two sub-stages.

Abstract

A three dimensional numerical study on bubble growth and merger in a micro-channel with diameter of 0.64 mm has been conducted. The working fluid is R134a and the wall material is steel. The inlet Reynolds number is set at 549 in order to keep the flow in laminar regime. Two different heat fluxes (14, and $28\frac{\text{kW}}{\text{m}^2}$) are supplied to the wall to heat up the fluid. The coupled level set and volume of fluid (CLSVOF) method is used to capture the distorted two-phase interface. An evaporation model is also implemented through UDF (User defined function). The combination of these two methods has successfully eliminated spurious velocities which is a common problem in two phase flow simulation. The boiling and merger processes are well-predicted by the simulation. It is found that the whole process can be divided to three sub-stages: sliding, merger, and post-merger. The dynamics and heat transfer are found to be different in these stages. The evaporation rate is much higher in the first two stages due to the thermal boundary layer effects.

Key words:

CFD, heat transfer, boiling, bubbles, evaporation, multi-phase flow, micro-channels, merger

Nomenclature list

Latin letters		Greek Letters	
A	area	α	volume fraction
C	coefficient	β	growth constant
c	specific heat	δ	thickness
Ca	capillary number	θ	contact angle
D	diameter	μ	viscosity
Eo	Eotvos number	ρ	density
F	force	σ	surface tension
G	mass flux	Φ	level set function
H	enthalpy		
k	thermal conductivity	Subscripts	
n	normal vector	b	bubble

* Corresponding author Tel: +46 (0)8 790 7453;

Email address: qingming@kth.se;bpalm@energy.kth.se

L	length	c	condensation
Mo	Morton number	d	diffusion
P	pressure	e	evaporation
Pr	Prandtl number	f	fluid
q	heat flux	g	gas
R_{int}	thermal resistance	l	liquid
Rg	gas constant	gr	grid
Re	Reynolds number	int	interface
T	temperature	o	operating condition
$\boldsymbol{U}$	velocity vector	v	vapor
Z	vertical distance	w	wall
We	Weber number	sat	saturation

1 Introduction

The study of micro-channels has attracted more and more attention during the last few decades. There are several reasons for this trend: advancements in MEMS (micro-electro -mechanical systems), fuel cells, cooling of micro-electronic chips, and also, compact heat exchangers.

While single phase flow in micro channel was studied comprehensively and the mechanism has been found similar to that of macro-scale channels, two phase flow in micro channels remains unclear[1]. New phenomena emerge and new methods are proposed in order to explain these phenomena as well as estimate key parameters such as pressure drop and boiling heat transfer coefficient.

The estimation of heat transfer coefficient of two phase convective boiling in micro channels can be divided in to four major methods: use of correlations from the literature [2], empirical method [3, 4], superposition model [5], and mechanistic modeling based on flow regimes [6, 7]. In the past, some researchers have argued that nucleate boiling is the dominant heat transfer mechanism in micro-channels due to the heat transfer coefficient's dependency on heat flux [8]. Others, on the contrary, have argued that the evaporation of the thin film between the bubbles and the wall plays a more important role [9].

Nowadays, it is widely accepted that the heat transfer has a strong link to flow patterns in micro-channels. In addition to the four most common flow patterns in macro channels -bubbly flow, slug flow, annular flow and mist flow, there are two new patterns only existing in micro channels[10-13]: confined bubbly flow and elongated bubbly/slug flow. These new flow patterns may have an important role to play in the heat transfer process.

In the last century, most of the two phase flow studies were conducted experimentally mainly due to the lack of robust numerical tools. Recently, the advancements in multiphase algorithms and computing capacity have facilitated numerical investigations of two-phase flow in micro-channels. For example, Kunkelmann and Stephan [14] numerically studied the transient heat transfer during nucleate boiling and the effect of contact line speed[15]. Gong and Cheng [16] examined periodic bubble nucleation, growth and departure from a heated surface by using the lattice Boltzmann method. Li et al[17] used the same tools to study the boiling curve and the effects of wettability on heat transfer. Agostini, Revellin [18] studied the velocity of an elongated bubble in an adiabatic micro-channel and proposed a predictive model based on these experiments. More recently, Consolini and Thome [19]proposed a one dimension model to predict the heat transfer coefficient of

2

confined (or elongated) bubbles. Sun, Xu [20] developed a new model based on VOF method for FLUENT. Magnini, Pulvirenti [21] developed a height function algorithm and investigated the effects of the leading elongated bubble. Liu, Palm [22] examined the dynamics and heat transfer of confined bubbles in a micro channel. They also studied the effect of contact angle and have found its importance on the bubble's shape.

All of the advancements listed above focus only on a single bubble during flow boiling. Not much attention has been paid to the study of bubbly flow involving interactions or even coalescence between two or more bubbles. As previous studies show, the interactions between two bubbles [23] , the wall influence[24] and the thermal effect [25] all play significant roles in bubble dynamics and make the study so complex that it is impossible to have analytical solutions. In addition, the scale of flow boiling in micro-channels is small which makes it difficult to study experimentally. Therefore numerical studies emerge as an important alternative. The aim of the present paper is to comprehensively study the transient process between two laterally placed bubbles in a vertical channel and try to explain their behavior and its role in heat transfer of convective boiling.

2 Numerical model

2.1 Coupling level set and volume of fluid method (CLSVOF)

There are several numerical tools to simulate phase-change flow, and two of them have been widely used: volume of fluid (VOF) and Level Set (LS). VOF[26] is a one-fluid algorithm deriving from continuum equations which enables it to have a mass-conservation nature. However, this causes relatively poor interface reconstruction due to a less accurate estimation of interface curvatures. In 1982Youngs [27] developed a piecewise linear scheme algorithm which can enhance the accuracy of the interface curvature calculation and this method has since then been widely accepted. Welch and Wilson [28] used this algorithm in conjunction with a mass transfer model and a surface tension model to successfully simulate horizontal film boiling. The level set method has a better estimation of interface curvature because it is a smooth function, but gives a poorer mass conservation, specifically when the interface experiences severe stretching or tearing. In order to overcome these problems, Sussman and Puckett [29] developed a coupled level set and VOF method (CLSVOF) where both the level set function and the volume fraction equations are solved. The interface is linearly reconstructed every time step from the volume fraction and then the level set function is reinitialized as the exact distance to this interface. This can significantly enhance the accuracy of mass conservation. This new method has better performance than both the level set and the VOF method, albeit at the price of complication. Tomar et al. [30] have studied a two dimension bubble growth in film boiling based on the CLSVOF method. Sato and Niceno [31] further extended it to a three dimension case. In order to reduce the difficulty of computation, especially in three dimensional cases, several similar methods with simpler implementation have been proposed. Van der Pijil et al.[32] suggested a mass-conserving level set method (MCLS) where the interface linear reconstruction is omitted. In addition, the VOF function is calculated from the level set function and is used to project the level set function in every time step. A coupled volume of fluid and level set (VOSET) method have been developed by Sun and Tao [33] where only the volume fraction equation is solved and the level set function is calculated from iterative geometric operation, which can reduce the computing load.

3

The governing equations of CLSVOF method are summarized as follows:

$$\frac{\partial \rho}{\partial t} + \nabla \cdot (\rho \boldsymbol{u}) = \dot{\rho} \tag{1}$$

$$\rho\left(\frac{\partial \boldsymbol{u}}{\partial t} + \boldsymbol{u} \cdot \nabla \boldsymbol{u}\right) = -\boldsymbol{\nabla}P + \boldsymbol{\nabla}\big(\mu(\boldsymbol{\nabla} \cdot \boldsymbol{u} + \boldsymbol{\nabla} \cdot \boldsymbol{u}^{T})\big) + \rho g + \boldsymbol{F_\sigma} \tag{2}$$

$$\rho C_p\left(\frac{\partial \boldsymbol{T}}{\partial t} + \boldsymbol{u} \cdot \boldsymbol{\nabla T}\right) = \boldsymbol{\Phi} + \boldsymbol{\nabla} \cdot (k\boldsymbol{\nabla}\mathrm{T}) + H_e \tag{3}$$

$$\frac{\partial \alpha}{\partial t} + \nabla \cdot (\alpha \boldsymbol{u}) = -\frac{\dot{\rho}}{\rho_v} \tag{4}$$

$$\frac{\partial \phi}{\partial t} + \nabla \cdot (\phi \boldsymbol{u}) = 0. \tag{5}$$

These are the continuity equation (1), the momentum equation (2), the energy equation (3), the volume fraction equation (4), and the level-set equation (5) respectively.

All the physical properties, such as density, viscosity and thermal conductivity, are the average value of all the phases in the cell and have the following form:

$$\Phi = \sum_{1}^{n} \Phi_i \alpha_i \ , \tag{6}$$

where α is the volume fraction of the primary phase (gas in this paper) in each computational cell.

$$\alpha(x,t) = \begin{matrix} 1 & if\ x\ \in primary\ phase \\ (0,1) & if\ x\ \in interface\ \Gamma \\ 0 & if\ x\ \in secondary\ phase \end{matrix} \ . \tag{7}$$

The level-set function ϕ is a signed distance, to the interface. Accordingly, the interface is defined as below.

$$\phi(x,t) = \begin{matrix} +|d| & if\ x\ \in primary\ phase \\ 0 & if\ x\ \in interface\ \Gamma \\ -|d| & if\ x\ \in secondary\ phase \end{matrix} \ , \tag{8}$$

where d is the shortest distance to the interface. The level set equation is solved to get the curvature and normal to the interface

$$\boldsymbol{n} = \frac{\nabla\phi}{|\nabla\phi|} \quad \boldsymbol{k} = \nabla \cdot \frac{\nabla\phi}{|\nabla\phi|} \ . \tag{9}$$

Then the surface tension force is found by the following equation

$$\boldsymbol{F_\sigma} = -\sigma\boldsymbol{k}\delta(\phi)\nabla\phi \ , \tag{10}$$

where

$$\boldsymbol{\delta}(\phi) = \begin{matrix} \dfrac{1 + cos(2\pi\phi/3L_{gr})}{2L_{gr}} & if\ |\phi| < 1.5\ L_{gr} \\ 0 & else \end{matrix} \ , \tag{11}$$

where L_{gr} is the minimum grid spacing.

2.2 Phase change model

The heat flux jump at the interface can be derived from kinetic theory[34] and be calculated from equation (12)

$$q_{e0} = \frac{T_{int} - T_{sat}}{R_{int}} \ , \tag{12}$$

4

where T_{int} is the interface temperature and R_{int} is the interfacial resistance defined by equation (13)

$$R_{int} = \frac{2 - C_e}{2C_e} \frac{\sqrt{2\pi R_{gas}}}{h_{lg}^2} \frac{T_{sat}^{3/2}}{\rho_v} \quad , \tag{13}$$

where C_e is the evaporation(or accommodation) coefficient, R_{gas} is the gas constant, h_{lg} is the latent heat and T_{sat} is the saturated temperature.

The original local evaporation rate can be calculated by equation (14)

$$\dot{\rho}_0 = \frac{N q_{e0} \alpha |\nabla \alpha|}{h_{lg}} \quad , \tag{14}$$

where N is a normalization factor to be determined from equation (15)

$$N = \frac{\oint_\Omega |\nabla \alpha| d\Omega}{\oint_\Omega \alpha |\nabla \alpha| d\Omega} \quad , \tag{15}$$

where Ω is a region enclosing a part of the interface. During numerical simulations, the liquid vapor interface is not shape and spreads about two or three cells. The spatial distribution across the interface plays a significant role in the calculation; a model with inappropriate local distribution can cause serious numerical instability. A smeared phase change model has been developed by Hardt and Wondra [35]. The principle of this model is to replace the original unstable interface evaporative rate ($\dot{\rho}_0$) by its normalized and smeared value (ρ_s). The first step is to calculate the smeared value by the diffusion equation (16)

$$\frac{\dot{\rho}_1 - \dot{\rho}_0}{\Delta t} = C_d \nabla^2 \dot{\rho}_0 \quad , \tag{16}$$

where C_d is the diffusive coefficient, Δt is the time step, $\dot{\rho}$ is the original evaporative rate and $\dot{\rho}_1$ is the smeared value. Then the complete interface mass source term in Eq.(1) can be determined by equation (17)

$$\dot{\rho} = N_l(1 - \alpha)\dot{\rho}_1 - N_v \alpha \dot{\rho}_1 \quad , \tag{17}$$

where N_l and N_v are normalization factors to be determined from equation (18)

$$N_v = \frac{\oint_\Omega \dot{\rho}_1 d\Omega}{\oint_\Omega \alpha \dot{\rho}_1 d\Omega} \quad N_l = \frac{\oint_\Omega \dot{\rho}_1 d\Omega}{\oint_\Omega (1 - \alpha \dot{\rho}_1) d\Omega} \quad . \tag{14}$$

The energy source H_e in Eq.(3) is obtained from equation (19)

$$H_e = \left[N_v \alpha c_{pv} - N_l(1 - \alpha)c_{pl} \right] \dot{\rho}_1 T - \dot{\rho} h_{lg} \quad . \tag{19}$$

More details of the implementation of this model can be found in Hardt's paper[35].

2.3 Discretization schemes

The simulation is performed by the commercial package ANSYS FLUENT 14.0. The pressure implicit splitting of operators (PISO) algorithm for pressure-velocity coupling is chosen owing to its higher accuracy for transient problems. For spatial discretization, the Green-gauss node based scheme for gradients produced lower magnitudes for spurious velocities. This is because of its better coupling between pressure and surface tension terms of the momentum equation. The pressure staggering

5

option (PRESTO!) scheme is chosen to interpolate pressure Due to its capability to achieve high order accuracy in smooth region while maintaining stable, non-oscillatory behavior at sharp discontinuities , the third order monotonic up stream centered scheme (MUSCL) is applied for momentum, energy and level-set discretization. The momentum and energy equation is solved by a first order implicit transient formulation. The Courant number is set to be always below 0.1, which makes the time step to vary between $1 * 10^{-8}$ and $5 * 10^{-7}$s.

The second upwind scheme is applied for user defined scalars. The evaporation model is implemented through User defined function (UDF) interface using C programming language. The meshes at and around the two-phase interface are of most interest. In order to precisely calculate both the evaporation and coalescence process, very high resolution meshes are needed in this region. In the present study, an adaptive mesh refinement algorithm is employed to achieve this goal. By using this method, the meshes in the interfacial region are refined dynamically –every 10 or 15 time steps-during the simulation. This enables accurate estimations for both evaporation and coalescence.

2.4 Boundary and initial conditions

A micro-channel with a diameter of 0.64 mm and length of 1.6 mm is studied in this paper. The sketch is shown in Fig.1. where the channel is vertically placed which means a $-z$ direction gravity vector. Cartesian coordinates are used with hexahedral grid. Two perpendicular and symmetric boundaries are defined at the center of the tube, so that only a quarter of the tube needs to be calculated. This would significantly reduce the computational time.

A single phase steady laminar simulation is performed at first and the steady result is used as the initial condition for the multiphase simulation. A constant heat flux ($14 \; or \; 28 \; \frac{kW}{m2}$) is supplied at the wall. No-slip velocity boundary condition is applied for the wall.

Uniform velocity and temperature boundary conditions are used at the inlet for the single phase simulation and the results are used as the inlet condition for the multiphase simulation. These values imply that the inertia force is neglegible compared to viscous force and it is a laminar flow regime since the Renolyds numbers of all cases are much smaller than 2100.The value of contact angle θ_{max} comes from experimental results of the flow of R134a through an aluminum wall [36].

For laminar flow, the thermal entry length is

$$\frac{L_e}{D} = 0.05 Re \cdot Pr \tag{20}$$

The thermal entry lengths corresponding to the given inlet velocity is $82 \; D$, which means all cases of this paper are in the thermal entry region. The wall temperature is above the saturated temperature depending on the position.

At the beginning of simulations, a pair of spherical "embryo bubbles" are introduced attach to the wall. Their distances from the inlet are 0.4 mm. As only bubbles bigger than a certain size (critical radius) can survive [37], all the embryo bubbles are initialized above this limit. The operating pressures are 7 bar (corresponding saturated temperatures is 300.15 K).

6

3 Verification and validation

3.1 Mesh independence

In order to check that the calculations are independent of mesh size, three cases with different mesh sizes have been studied. The minimum mesh sizes are set to $\frac{D}{64}, \frac{D}{128}$, and $\frac{D}{256}$, respectively, where D is the channel diameter. As Fig.2 shows, the case with a minimum mesh size of $\frac{D}{64}$ overestimates the bubble's volume. In addition, it has a very poor interface reconstruction. As shown in Fig.2, this mesh size ($\frac{D}{64}$) produces additional bubbles which are not only unphysical but also do not appear in the other two cases ($\frac{D}{128}$, and $\frac{D}{256}$.) The difference, both in terms of the bubble shape and the bubble growth (Fig.2), for the other two mesh sizes ($\frac{D}{128}$, and $\frac{D}{256}$.) are negligible. In order to save on computational time, the minimum mesh size of $\frac{D}{128}$ is utilized for all cases.

3.2 Test case 1: single bubble growth in super-heated liquid

Scriven[38] has studied a bubble growing in a super-heated liquid and derived an analytical expression for the bubble radius as a function of time.

$$R(t) = 2\,\beta\sqrt{\alpha t}\ ,$$ (21)

where β is the growth constant and α is the liquid thermal diffusivity

$$\beta = \sqrt{\frac{3}{\pi} \frac{\Delta T}{\frac{\rho_g}{\rho_l}(\frac{L}{c_l} + (\frac{c_l - c_g}{c_l})\Delta T)}}\ .$$ (22)

In order to verify the phase change model of this paper, a spherical bubble with an initial radius of 0.1 mm is placed in superheated liquid in a unbounded container. With this radius the bubble is big enough such that the difference in saturation temperature across the interface can be neglected. Gravity is zero and the pressure is set to be 0.84 bar. At the beginning, the velocity field is set to zero, the temperature inside the bubble is equal to the saturation temperature (T_{sat}) and outside the temperature is $T_{sat} + 5K$. In order to save on computation time, the central line of the tube is set as an axisymmetric boundary. As Fig.3 indicates, the simulated bubble radius has a reasonably good agreement with the analytical solution.

3.3 Test case 2: Motion of a Taylor bubble in a micro-channel

Long bubbles moving in a viscous fluid in narrow channels is a common phenomenon in industrial applications. This system has been extensively studied by means of both experiments and modeling. Bretherton [39] has derived a theory by which the thickness of the thin film trapped between the wall and the bubble can be calculated from the lubrication approximation. According to this theory, the thin fluid film region between the bubble and the wall is divided into three parts: the leading nose with a varying thickness, the middle body with nearly constant film thickness, and the bottom meniscus with a very thin fluid film. The lubrication theory has been developed by several researchers in the past few decades. A modified version specifically for micro-channels was proposed by Han and Shikazono [40] and the governing relations are summarized in equations (23, 24 and 25).

$$\frac{\delta}{D} = \frac{0.67Ca^{2/3}}{1 + 3.31Ca^{2/3} + 0.504Ca^{0.672}Re^{0.589} - 0.352We^{0.629}}$$ (23)

7

$$Ca = \frac{\mu * \boldsymbol{u}_b}{\sigma} \tag{24}$$

$$We = Ca * Re, \tag{25}$$

where δ is the thin film thickness, Ca is the capillary number and We is the Weber number.

In order to validate the code's ability for surface tension estimation, an adiabatic R134a bubble in a channel with a diameter of 0.64 mm is studied. An axi-symmetric boundary condition is applied. The initial film thickness between the bubble and the tube wall is for all cases 0.02 mm. The initial bubble consists of a cylinder with a diameter of 0.6 mm , a length of 1.28 mm and a hemispherical head with a diameter of 0.6 mm. Both the inlet and outlet velocities are kept at 0.1 m/s. Certain physical properties such as viscosity, surface tension and density are adjusted in order to get different capillary numbers while the Reynolds number is kept constant (Table 1). All cases are run till the bubble terminal velocities reach a constant value. These velocities can be predicted by Taylor's law [41]

$$\frac{u_b - u_f}{u_b} \tag{26}$$

where v_l is the average fluid velocity.

The steady state shapes of the bubbles are plotted for different capillary numbers in Fig.4. The figure clearly shows that the liquid film thickness increases with increasing capillary numbers, which is in agreement with the classical lubrication theory. The shape of the rear end of the bubble is another phenomenon which has been confirmed by earlier experimental work [42]. It should be noted that the sketch is not strictly 1:1 imaging of the bubbles, but with a compression of the *x*-axis, which means the real difference between film thicknesses is smaller than as indicated by the figure.

The numerical results of film thickness and terminal velocities are compared with Han's correlation and Taylor's law at different capillary numbers. As Figure 5 illustrates, these two values have good agreement in all cases except only a slight underestimation of the liquid film thickness for the highest capillary number, 0.069. Considering that all the cases studied in this paper have a capillary number less than 0.01, the code is proved to be reliable.

3.4 Test case 3: two bubbles rise in line and coalesce

The third test case involves the co-axial coalescence of two spherical gas bubbles in an initially quiescent liquid in an axisymmetric domain. Initially two spherical gas bubbles with the same diameter $d_0 = 10 \, mm$ are placed on the symmetry axis at the axial positions $z = 1.5 \, d_0$ and $z = 3d_0$, respectively. The distance between centers of the two bubbles is $1.5d_0$. The size of the domain is $4d_0 \times 8 \, d_0$. The calculations are carried out on a $0.2 \times 0.2 \, mm$ grid. The properties of the fluid are set in accordance to the experimental settings of Brereton and Korotney [43] and are listed in Table 2. The liquid to gas density and viscosity ratios are 100, which is greater than the value of most refrigerants.

Fig.6 illustrates the present numerical snapshots comparing to previous experimental results [43]. The interfaces of the two bubbles are well-captured by the present numerical algorithm. The instantaneous Reynolds number of the leading bubble calculated from the numerical simulation is always close to 50, which is the experimental value obtained by Bhaga and Weber[44].

8

3.4 Test case 4: Two bubbles rising side by side and coalescing

Two bubbles rising side by side and merging laterally has been widely observed in both industrial applications and experimental studies. In this section a comparison between our simulation and a visualization study conducted by Owhaib [45] under the same boundary and operating conditions has been made. This case concerns two pairs of bubbles sliding along a wall in upward R134a flow inside a micro tube with a diameter of 0.64 mm. The inlet mass flux is $G = 112\ kg * \frac{m^2}{s}$ and the wall heat flux is ($q = 5\frac{kW}{m^2}$). The saturation temperature is 300.15 K which has a corresponding saturation pressure of 7 bar. As Fig.7 shows, the movement and merging process of the bubbles have been successfully simulated. It indicates that the whole process can be roughly divided to three sub-stages: sliding, merging and post-merging. At the first stage, bubbles are close to the wall and absorb heat from the super-heated liquid close to the wall. The lift force is not big enough to take the bubbles from the wall. After a while the leading pair of bubbles have become big enough to "touch" each other and they start to merge. The merging process is an extremely quick process- it takes only a few milli seconds. The capillary force as well as the lift forcedrag the new merging bubble from the wall. While the leading bubble pair merges with each other, the bubbles in the trailing one have not grown big enough within the computational time. Previous studies[44, 46] also have shown that trailing bubbles usually do not have a significant effect on leading ones, therefore the trailing bubbles will be omitted from the analysis in the following sections of the present paper. It should be noted that the comparison is not a rigorous quantitative one: The bubble size and time span between each picture in Fig.7 are not exactly the same. Nevertheless, the difference is small. Besides this case is similar to the studying cases in Section 4, but with lower heat flux and smaller initial bubble sizes.

4 Results and discussions

4.1 Dynamics of the growing and merging process

Two bubbles rising side by side in an upward R134a flow in a micro channel with a diameter of 0.64 mm will be studied in this section. The flow domain and boundary conditions have been mentioned in Section 2.4. As Fig. 8 indicates, buoyancy and drag force push bubbles moving upwards. At the same time the lift force push bubbles away from the wall and evaporation of super-heated liquid at the bubble interface makes them expanding. At a certain point, when the bubbles' diameters are close to the radius of the channel, the two bubbles begin to merge. During this merging period, the surface tension force pulls the two bubbles away from the wall. As stated before, the merging process is a very quick process which takes less than one milli second in the present study. The new merging bubble is expanding dramatically in the radial direction first (4.5ms for q=28 kW/m², and 6.4ms for q=14 kW/m²), and then quickly contract (4.9ms for q=28 kW/m², and 6.7ms for q=14 kW/m²).

Velocity fields around the bubbles (Fig. 9) are affected by both bubble growth and movements. The effect is not very significant before the merger since the velocity field is still relatively uniform at this time (1.9ms). The only observed effect is the increased speed of the fluid near the top of the bubbles, which is mainly due to the bubble growth. On the contrary, the merging process distorted the velocity field around bubbles. At the middle stage of the merger (4.5 ms), the expansion of the bubble along the centerline causes an obvious vortex between the top of bubbles and the wall. And in the end of merger (4.9 ms), the momentum forces in the axial direction distort the bubble and pull it from the wall..

9

The bubbles are affected by the merging process too. The bubbles' vertical (axial) and radial velocities during the whole process are plotted against time in Fig.10 and Fig.11. The minus values of radial velocities denote that they are moving away from the wall (or toward the channel center). As can be seen from Fig.9 the bubble's velocity is not even on the surface. Surfaces close to the wall has lower velocity before the merger. As the bubbles start to merge, the velocity at the merging part rises to a much higher value than other parts while the velocity near the channel wall remains as the lowest. However, as the merging process progresses, the velocity at the part close to the channel wall also increases to values as high as those at the top of the bubble. The

lowest velocity appears at the bottom of the new merging bubble.

The average vertical and radial velocities of the bubbles are illustrated in Fig.11. Before the merger, the increase of the vertical velocities is mainly due to the bubbles' radial movement. Since the velocity is higher in the tube center, a movement towards it would increase the bubbles velocity. The sudden change of vertical velocity comes from the merger. The radial velocity also has the same trend with a higher magnitude. The vertical velocity of the bubbles increased about 30% within 0.5 milliseconds while the radial velocity increased more than 10 times in the same time period, but within 1 millisecond the velocity was back to the original value close to zero.

4.2 Heat transfer

The bubble growth and merger also have strong effects on the temperature field and the heat transfer. The temperature field around the bubbles at the XZ plane is plotted in Fig.11. Before the merger, the bubbles already have a very significant effect on the thermal boundary layer separating it from the wall. Specifically, the temperature in this region is decreased mainly due to the bubbles' evaporation . As the bubble moves upwards, the thermal boundary layer, with lower velocity than the bubble, is continuously cooled as the superheated liquid evaporates into the bubble. It should be noted that this effect seems to decrease as the bubbles move away from the wall during its upward movement. At the middle period of the bubbles' merging process (4.5 ms), the new merging bubble expands in X (and –X) direction along the centerline and this seems to decrease the thickness of the thermal boundary layer. The last stage of the merger actually makes the thermal boundary layer thicker due to the contraction of the new merging bubble. In other words, hot fluid is first pushed away, and then sucked bac along the surface and in towards the center close to the bubble. .

The wall temperature is plotted in Fig.12. It confirms the analysis based on the temperature contour of the XZ plane. At the beginning (2.0 ms), the lowest value of the wall temperature (at the point closest to the bubbles) is very close to the saturation temperature (300.15 K). As the bubbles move upwards and towards the channel center, the wall temperature increases. At the

middle of the merger period (4.5 ms), the wall temperature close to the bubble (Z=0.82 mm) decreases slightly. And in the end of the merger (4.9 ms), the temperature in the corresponding region (Z=0.87 mm) increases.

The radial fluid temperatures can be studied in more detail in the right part of Fig. 12. A line through the center of the bubbles, with a direction perpendicular to the YZ plane is chose (X direction). Since the bubbles are moving upwards, this line is also changing its position and has an increasing Z position at different times (0.56 0.76 0.82 0.87 mm corresponding to different times). The variation of the line temperature in the X direction is plotted in Fig.12. At the beginning (2.0 ms), the thermal

10

boundary layer is very thin (0.01 mm) and the maximum value of the line temperature is very close to the saturation temperature (300.15 K). In the merging process, both values increase-boundary layer grows to 0.03 mm and maximum value of line temperature increases to as high as 317 K. At the end of the merging process, these two values increase further to 0.15 mm and 320 K respectively.

As discussed in Section 3.2, evaporation is a temperature controlled phenomenon. In a uniform super-heated fluid, for a given fluid, the bubble growth rate or evaporation rate is simply a function of time, and super-heat degree. Bubble growth in a micro channel, however, is a rather complicated process due to the uneven temperature field within the thermal boundary layer. Two bubbles with interactions will add even more complexity because even the bubble movement becomes unpredictable by asymptotic equations.

The contour of the evaporation rate at the bubbles is plotted in Fig.13. It shows how the evaporation rate distributes and how it changes at different stages. It is not surprising that most evaporation is taking place at the interface near the channel wall. The highest evaporation rate seems to be at the upper inner (close to the wall) part of these interfaces due to a higher degree of super-heat. Both evaporation rate and interface area decrease with the moving and merging of bubbles.

The bubble volume and the total evaporation rate are plotted in Fig.14. It is clearly shown that a higher wall heat flux leads to a higher bubble growth rate. The evaporation rate has the same trend and decreases with time. The evaporation rate at the heat flux ($q = 28 \frac{kW}{m^2}$) has even declined to zero at the end of the merging. That means that the new merged bubble is completely surrounded by saturated fluid. On the contrary, the case with a lower heat flux ($q = 14 \frac{kW}{m^2}$) still have a low but non-zero evaporation rate. This is because the new-merged bubble in this case is wider (in X direction) at this time, and therefore still has a small part in the super-heated fluid of the thermal boundary layer. .

5 Conclusions

A three dimensional numerical study on the bubble growth and merger during convective boiling in a micro-channel with diameter of 0.64 mm has been conducted. Combination of the CLSVOF method and the phase change model has proved to be a reliable tool. This has been shown by validating against existing analytical models as well as against experimental results. Specifically, Test case 1 has validated the phase change model, Test case 2 has proved the surface tension model is reliable, then Test case 3 has shown the ability of modeling of vertical coalescence and Test case 4 has confirmed the robustness of the model on lateral coalescence by comparing with a visualization result.

The dynamics and heat transfer of the bubbles during sliding and merging process have been investigated in detail. The results show that the process is very complicated which confirm the impression that this sort of problems may not be solved analytically. It is also found that this transition process plays a key role in the heat transfer of flow boiling in micro channels. The following conclusions can be drawn based on the study:

1 The transition process can be roughly divided into three stages: sliding, merging and post-merging stages. The latter two stages are both extremely fast processes which takes less than one millisecond. The dynamics and heat transfer are very different in these three stages.

11

2 Bubbles move upwards and migrate away from the wall at the same time as they grow due to the heat transferred from the surrounding super-heated fluid in the thermal boundary layer. During this time, bubbles have relatively high growth rate but low velocity (both vertical and transverse velocities). The thermal boundary layer is highly distorted and thinned close to the bubble during this time and therefore a relatively high rate of heat transfer is taking place between the fluid and channel wall.

3 When bubbles are big enough to meet each other, they will start to merge. Surface tension seems to be the dominant force in this stage. The force is so strong that the forming of a new bubble can be done within 1 millisecond. The expansion of bubble along the radial direction makes the bubble protrude into the thermal boundary layer and hence enhances heat transfer. During this stage the bubble have relatively moderate growth rate.

4 After that, the bubble contracts, also at a very fast pace and most of the bubble is left out of the thermal boundary layer. The final shape depends on the bubble volume. It also pulls the fluid from the wall which makes the thermal boundary layer thicker. During this post-merging stages the bubble have very low (even zero) bubble growth rate.

Acknowledgement

References

1. Fan, L.-W., et al., *Subcooled Pool Film Boiling Heat Transfer From Spheres With Superhydrophobic Surfaces: An Experimental Study.* Journal of Heat Transfer, 2016. **138**(2): p. 021503.
2. Lazarek, G. and S. Black, *Evaporative heat transfer, pressure drop and critical heat flux in a small vertical tube with R-113.* International Journal of Heat and Mass Transfer, 1982. **25**(7): p. 945-960.
3. Kandlikar, S.G. and P. Balasubramanian, *An Extension of the Flow Boiling Correlation to Transition, Laminar, and Deep Laminar Flows in Minichannels and Microchannels.* Heat Transfer Engineering, 2004. **25**(3): p. 86-93.
4. Ribatski, G., et al., *On the Prediction of Heat Transfer in Micro-Scale Flow Boiling.* Heat Transfer Engineering, 2007. **28**(10): p. 842-851.
5. Zhang, W., T. Hibiki, and K. Mishima, *Correlation for flow boiling heat transfer in mini-channels.* International Journal of Heat and Mass Transfer, 2004. **47**(26): p. 5749-5763.
6. Thome, J.R., V. Dupont, and A.M. Jacobi, *Heat transfer model for evaporation in microchannels. Part I: presentation of the model.* International Journal of Heat and Mass Transfer, 2004. **47**(14-16): p. 3375-3385.
7. Cioncolini, A., et al., *Microscale Adiabatic Gas–Liquid Annular Two-Phase Flow: Analytical Model Description, Void Fraction, and Pressure Gradient Predictions.* Heat Transfer Engineering, 2010. **31**(4): p. 310-320.
8. Kandlikar, S.G., *Heat Transfer Mechanisms During Flow Boiling in Microchannels.* Journal of Heat Transfer, 2004. **126**(1): p. 8.
9. Thome, J.R. and L. Consolini, *Mechanisms of Boiling in Micro-Channels: Critical Assessment.* Heat Transfer Engineering, 2010. **31**(4): p. 288-297.
10. Owhaib, W. and B. Palm, *Experimental investigation of single-phase convective heat transfer in circular microchannels.* Experimental Thermal and Fluid Science, 2004. **28**(2): p. 105-110.

12

11. Maqbool, M.H., B. Palm, and R. Khodabandeh, *Boiling heat transfer of ammonia in vertical smooth mini channels: Experimental results and predictions.* International Journal of Thermal Sciences, 2012. **54**: p. 13-21.

12. Moreno Quibén, J. and J.R. Thome, *Flow pattern based two-phase frictional pressure drop model for horizontal tubes. Part I: Diabatic and adiabatic experimental study.* International Journal of Heat and Fluid Flow, 2007. **28**(5): p. 1049-1059.

13. Celata, G., et al., *Flow pattern analysis of flow boiling inside a 0.48 mm microtube.* International Journal of Thermal Sciences, 2012. **58**: p. 1-8.

14. Kunkelmann, C. and P. Stephan, *Numerical simulation of the transient heat transfer during nucleate boiling of refrigerant HFE-7100.* International Journal of Refrigeration, 2010. **33**(7): p. 1221-1228.

15. Kunkelmann, C., et al., *The effect of three-phase contact line speed on local evaporative heat transfer: Experimental and numerical investigations.* International Journal of Heat and Mass Transfer, 2012. **55**(7-8): p. 1896-1904.

16. Gong, S. and P. Cheng, *Lattice Boltzmann simulation of periodic bubble nucleation, growth and departure from a heated surface in pool boiling.* International Journal of Heat and Mass Transfer, 2013. **64**(0): p. 122-132.

17. Li, Q., et al., *Lattice Boltzmann modeling of boiling heat transfer: The boiling curve and the effects of wettability.* International Journal of Heat and Mass Transfer, 2015. **85**: p. 787-796.

18. Agostini, B., R. Revellin, and J.R. Thome, *Elongated bubbles in microchannels. Part I: Experimental study and modeling of elongated bubble velocity.* International Journal of Multiphase Flow, 2008. **34**(6): p. 590-601.

19. Consolini, L. and J.R. Thome, *A heat transfer model for evaporation of coalescing bubbles in micro-channel flow.* International Journal of Heat and Fluid Flow, 2010. **31**(1): p. 115-125.

20. Sun, D.-L., J.-L. Xu, and L. Wang, *Development of a vapor–liquid phase change model for volume-of-fluid method in FLUENT.* International Communications in Heat and Mass Transfer, 2012. **39**(8): p. 1101-1106.

21. Magnini, M., B. Pulvirenti, and J.R. Thome, *Numerical investigation of hydrodynamics and heat transfer of elongated bubbles during flow boiling in a microchannel.* International Journal of Heat and Mass Transfer, 2013. **59**(0): p. 451-471.

22. Liu, Q., B. Palm, and H. Anglart. *Simulation on the flow and heat transfer characteristics of confined bubbles in micro-channels*. in *ASME 2012 10th International Conference on Nanochannels, Microchannels, and Minichannels collocated with the ASME 2012 Heat Transfer Summer Conference and the ASME 2012 Fluids Engineering Division Summer Meeting*. 2012. American Society of Mechanical Engineers.

23. Legendre, D., J. Magnaudet, and G. Mougin, *Hydrodynamic interactions between two spherical bubbles rising side by side in a viscous liquid.* Journal of Fluid Mechanics, 2003. **497**: p. 133-166.

24. Magnaudet, J., S. Takagi, and D. Legendre, *Drag, deformation and lateral migration of a buoyant drop moving near a wall.* Journal of Fluid Mechanics, 2003. **476**: p. 115-157.

25. Legendre, D., J. Borée, and J. Magnaudet, *Thermal and dynamic evolution of a spherical bubble moving steadily in a superheated or subcooled liquid.* Physics of Fluids (1994-present), 1998. **10**(6): p. 1256-1272.

26. Hirt and Nichols, *Volume of fluid (VOF) method for the dynamics of free boundaries.* 81.

27. Youngs, D.L., *Time-dependent multi-material flow with large fluid distortion.* Numerical methods for fluid dynamics, 1982. **24**: p. 273-285.

28. Welch, S.W.J. and J. Wilson, *A Volume of Fluid Based Method for Fluid Flows with Phase Change.* Journal of Computational Physics, 2000. **160**(2): p. 662-682.

29. Sussman, M. and E.G. Puckett, *A Coupled Level Set and Volume-of-Fluid Method for Computing 3D and Axisymmetric Incompressible Two-Phase Flows.* Journal of Computational Physics, 2000. **162**(2): p. 301-337.

13

30. Tomar, G., et al., *Numerical simulation of bubble growth in film boiling using a coupled level-set and volume-of-fluid method.* Physics of Fluids, 2005. **17**(11): p. 112103.

31. Sato, Y. and B. Ničeno, *A sharp-interface phase change model for a mass-conservative interface tracking method.* Journal of Computational Physics, 2013. **249**(0): p. 127-161.

32. van der Pijl, S.P., et al., *A mass-conserving Level-Set method for modelling of multi-phase flows.* International Journal for Numerical Methods in Fluids, 2005. **47**(4): p. 339-361.

33. Sun, D.L. and W.Q. Tao, *A coupled volume-of-fluid and level set (VOSET) method for computing incompressible two-phase flows.* International Journal of Heat and Mass Transfer, 2010. **53**(4): p. 645-655.

34. Schrage, R.W., *A theoretical study of interphase mass transfer*1953: Columbia University Press.

35. Hardt, S. and F. Wondra, *Evaporation model for interfacial flows based on a continuum-field representation of the source terms.* Journal of Computational Physics, 2008. **227**(11): p. 5871-5895.

36. Vadgama, B. and D.K. Harris, *Measurements of the contact angle between R134a and both aluminum and copper surfaces.* Experimental Thermal and Fluid Science, 2007. **31**(8): p. 979-984.

37. Carey, V.P., *Liquid-vapor phase-change phenomena*. Applied Mechanics Reviews. Vol. 45. 1992.

38. Scriven, L.E., *On the dynamics of phase growth.* Chemical Engineering Science, 1959. **10**(1–2): p. 1-13.

39. Bretherton, F., *The motion of long bubbles in tubes.* Journal of Fluid Mechanics, 1961. **10**(02): p. 166-188.

40. Han, Y. and N. Shikazono, *Measurement of the liquid film thickness in micro tube slug flow.* International Journal of Heat and Fluid Flow, 2009. **30**(5): p. 842-853.

41. Taylor, G., *Deposition of a viscous fluid on the wall of a tube.* Journal of Fluid Mechanics, 1961. **10**(02): p. 161-165.

42. Aussillous, P. and D. Quéré, *Quick deposition of a fluid on the wall of a tube.* Physics of Fluids (1994-present), 2000. **12**(10): p. 2367-2371.

43. Brereton, G. and D. Korotney, *Coaxial and oblique coalescence of two rising bubbles.* Dynamics of bubbles and vortices near a free surface, AMD, 1991. **119**.

44. Bhaga, D. and M. Weber, *In-line interaction of a pair of bubbles in a viscous liquid.* Chemical Engineering Science, 1980. **35**(12): p. 2467-2474.

45. Owhaib, P., *Experimental Heat Transfer, Pressure Drop, and Flow Visualization of R 134a in Vertical MiniMicro Tubes.* PhD Thesis, 2009.

46. Magnini, M., B. Pulvirenti, and J.R. Thome, *Numerical investigation of the influence of leading and sequential bubbles on slug flow boiling within a microchannel.* International Journal of Thermal Sciences, 2013. **71**: p. 36-52.
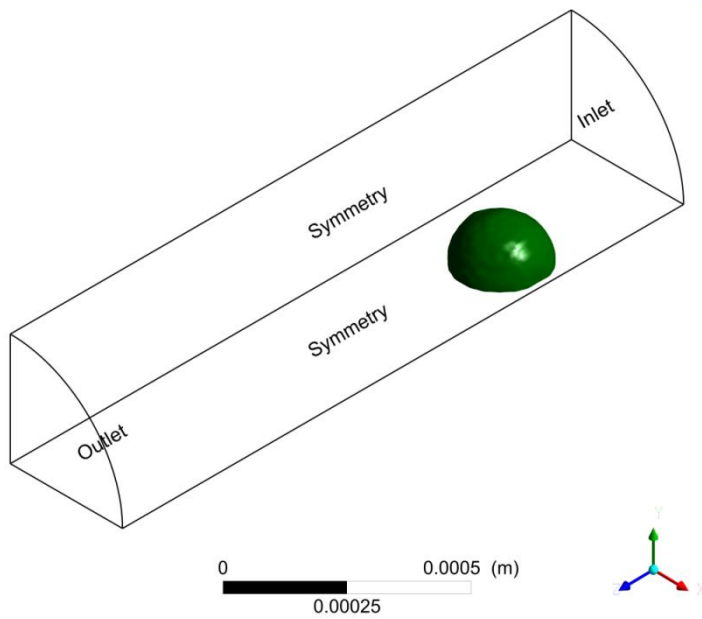
14

Figure 1. The simulation domain is a 1.6 mm long cylindrical channel with a diameter of 0.64 mm. Bubbles' initial radius are 0.11mm and is placed 0.4 mm from the inlet. Inlet Reynolds number is 549 and the wall heat flux is 14 or 28 $\frac{kW}{m^2}$. Saturated temperature is 300.15 K Blue arrow points in the Z direction, red arrow in the X direction and green arrows in the Y direction.
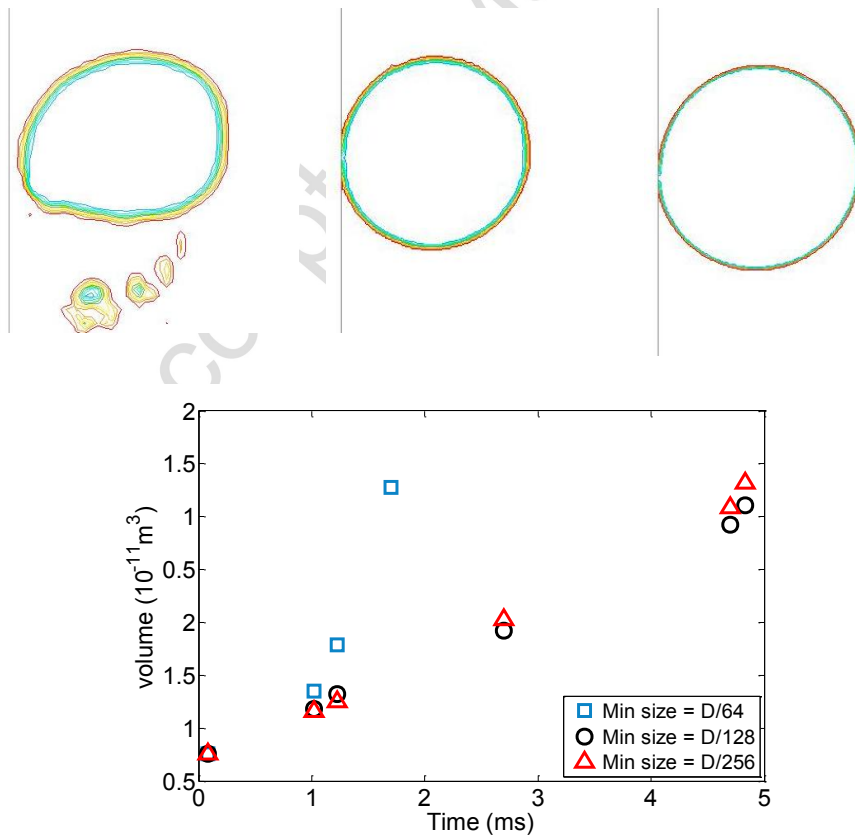

Figure 2. Shapes of a bubble's cross section at time 0.12 ms corresponding to different minimum mesh sizes (top three figures from left to right are $\frac{D}{64}, \frac{D}{128}$, and $\frac{D}{256}$ respectively) and bubble growth with different mesh sizes. Boundary conditions: constant wall heat flux $q = 5\frac{kW}{m2}$, mass flux $G = 56\ kg * \frac{m2}{s}$, saturation temperature: $T_{sat} = 300.15\ K$

15
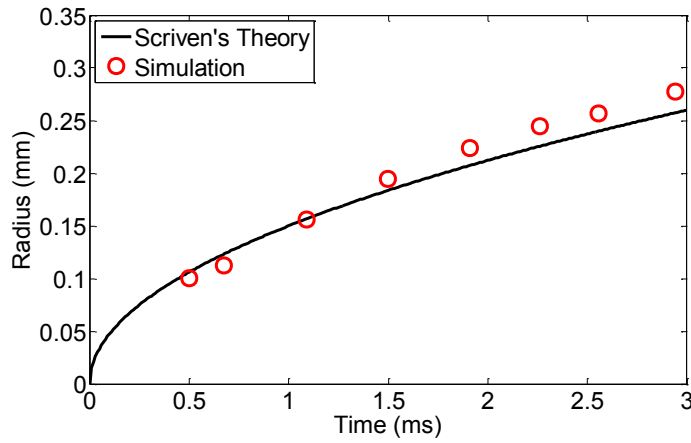
Figure 3. Radius of bubbles over time compared with Scriven's theory. Working fluid: *R134a.* Super heat degree of liquid: $5\ K$, and the operating pressure is $0.84\ bar$.
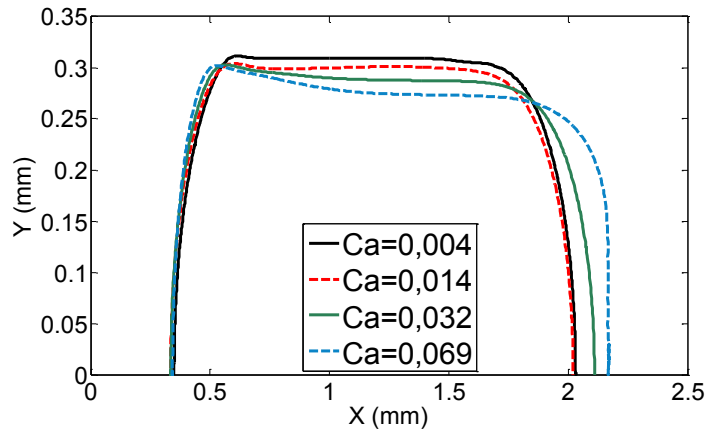
Figure 4. Bubbles shapes at different Capillary numbers. Operating conditions: $\text{Re} = 7.8$, original bubble radius = 0.32 mm, fluid velocity = $0.1\frac{\text{m}}{\text{s}}$, gravity = $9.8\text{m}/s^2$
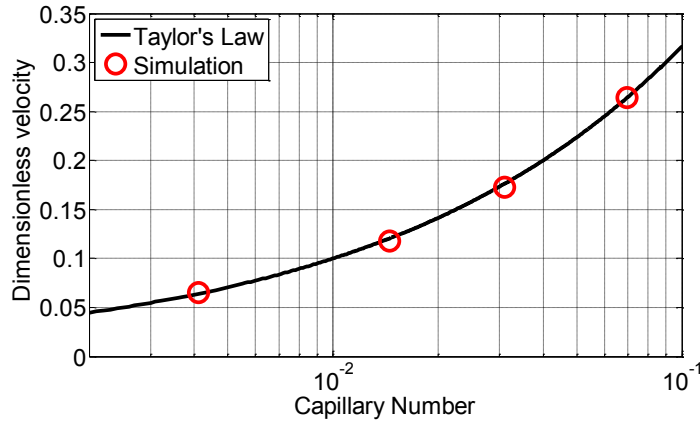

16
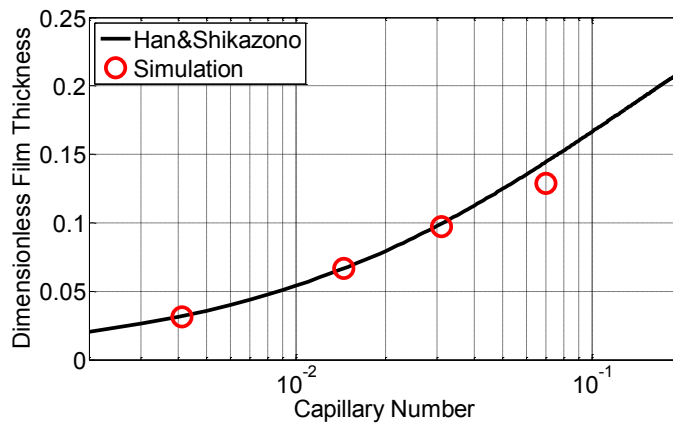
Figure 5. Top: Bubbles' dimensionless film thickness $\left(\frac{2\delta}{D}\right)$ Vesus Capillary numbers. The black solid line represents the analytical solution by Han & $Shikazono's$ empirical correlations, , and the red circles denote the simulation data. Bottom: Bubbles' dimensionless terminal velocities vs capillary number. the black solid line represents the lubrication theory, and the red circles are the results of the simulation. The dimensionless velocity is defined as $\frac{u_b - u_f}{u_b}$, where u_b is the terminal velocities of bubbles and u_f is the mean fluid velocity. Operating conditions: $Re = 7.8$, original bubble radius $= 0.32$ mm, fluid velocity $= 0.1\frac{m}{s}$, gravity $= 9.8$m/s2
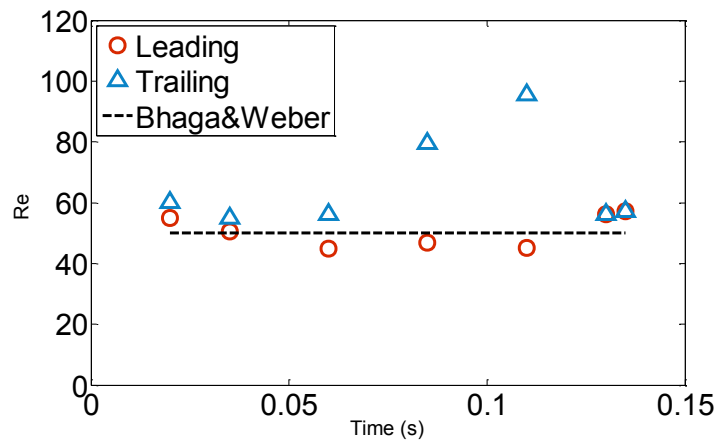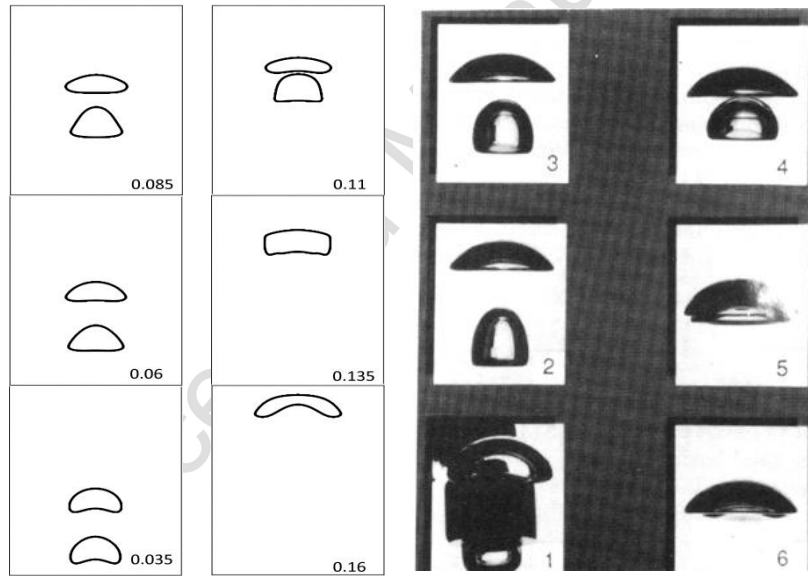
Figure 6. Snapshots at different times of the co-axial coalescence of two initially spherical bubbles of 10 mm diameter released from positions $(0.0, 15.0 \text{ mm})$ and $(0.0, 30.0 \text{ mm})$ in an initially quiescent liquid in a cylindrical column of 40.0×80.0 mm, using a 0.2×0.2 mm grid and a time step of 5×10^{-5} s. Eo $= 16$ and Mo $= 2 \times 10^{-4}$. Included are the simulation (the numbers in the pictures indicate the time in seconds) and photographs (time difference between subsequent photographs is 0.03 s) taken from Brereton and Korotney [43].
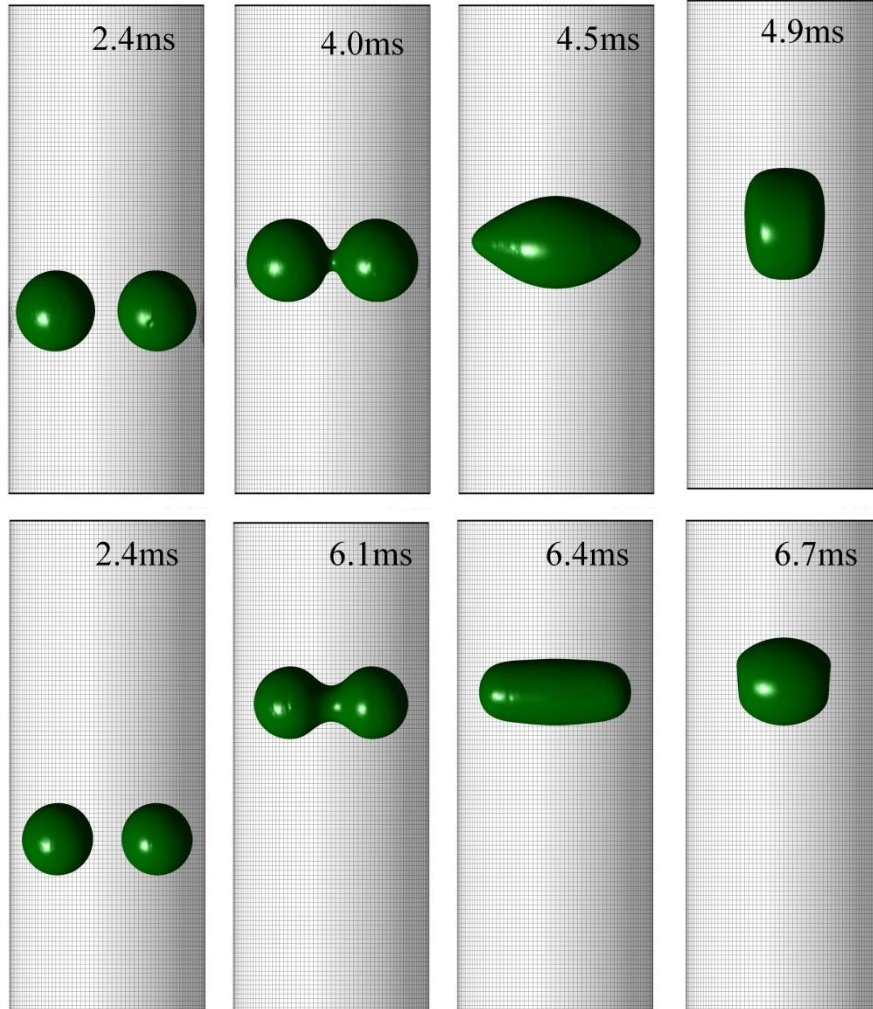
Figure 8. Changes in bubble shape with time.

Constant wall heat flux $q = 28 \, (top) \, and \, 14 \, (bottom) \frac{kW}{m^2}$, inlet Re = 549, saturation temperature $Tsat = 300.15 \, K$.
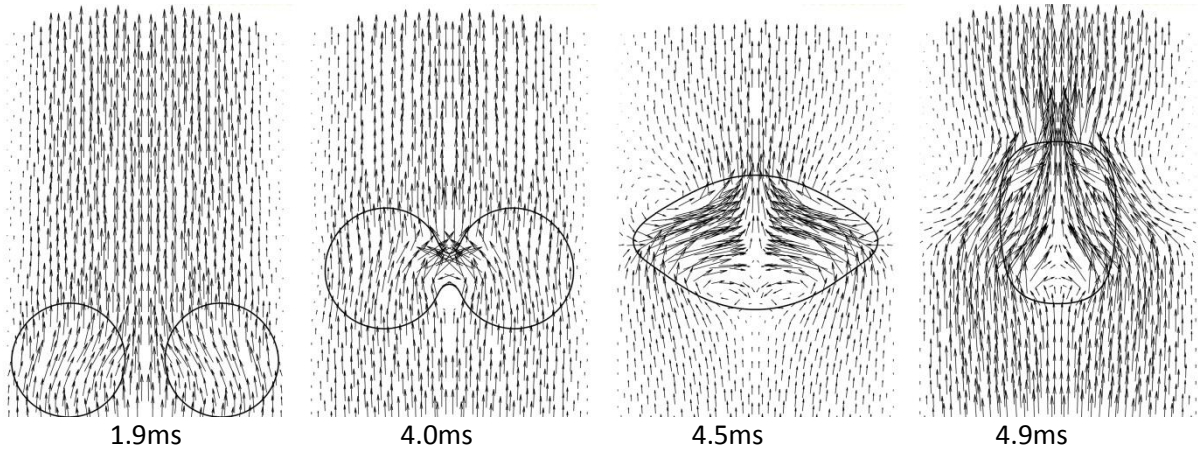
18

Figure 9. Fluid velocity at the central plane at different stages of the merging process. Boundary conditions: constant wall heat flux $q = 28\frac{kW}{m^2}$, inlet Re = 549, saturated temperature $Tsat = 300.15\,K$.
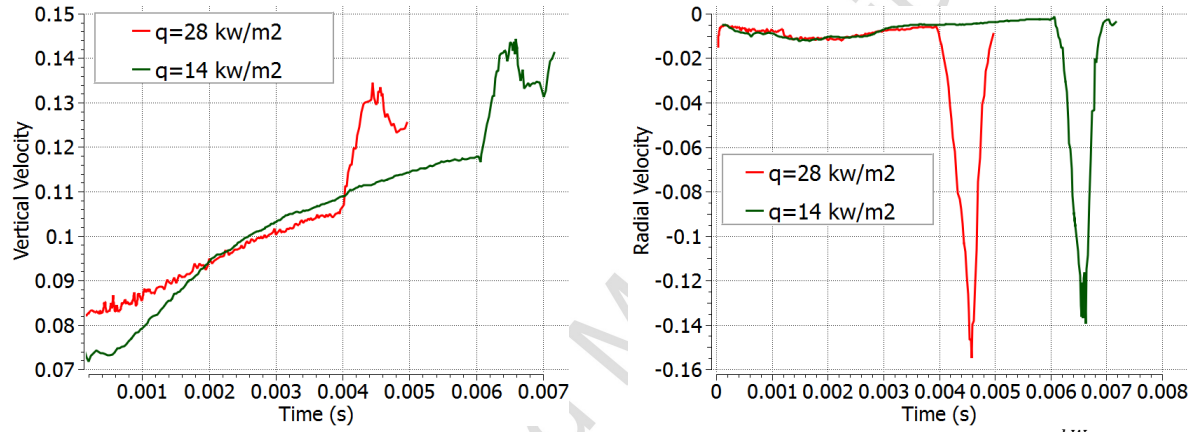

Figure 10. Bubble velocity at different stages. Boundary conditions: constant wall heat flux $q = 14\ and\ 28\frac{kW}{m^2}$, inlet Re = 549, saturation temperature $= 300.15\,K$.
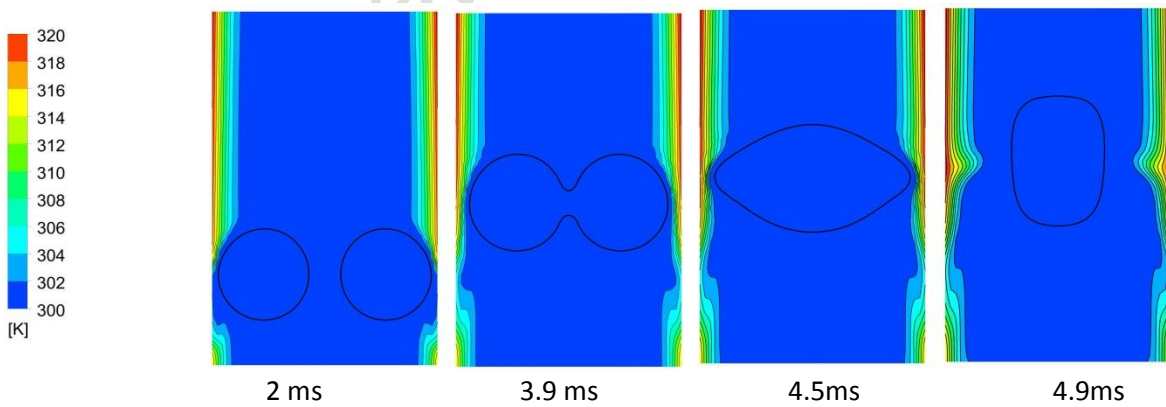

Figure 11. Temperature contour at different stages. Boundary conditions: constant wall heat flux: $q = 14, 28\frac{kW}{m^2}$, inlet Re = 549, and saturation temperature $Tsat = 300.15\,K$.
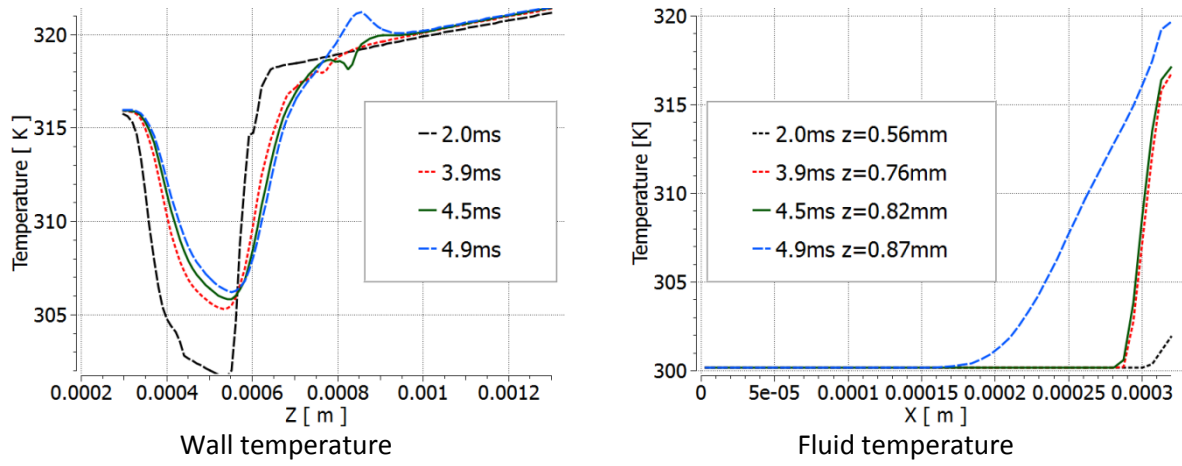
19

Figure 12. Wall (left) and fluid temperature (right) at different stages. Boundary conditions: constant wall heat flux $q = 14, 28 \frac{kW}{m^2}$, inlet Re = 549, and saturation temperature $Tsat = 300.15\ K$.
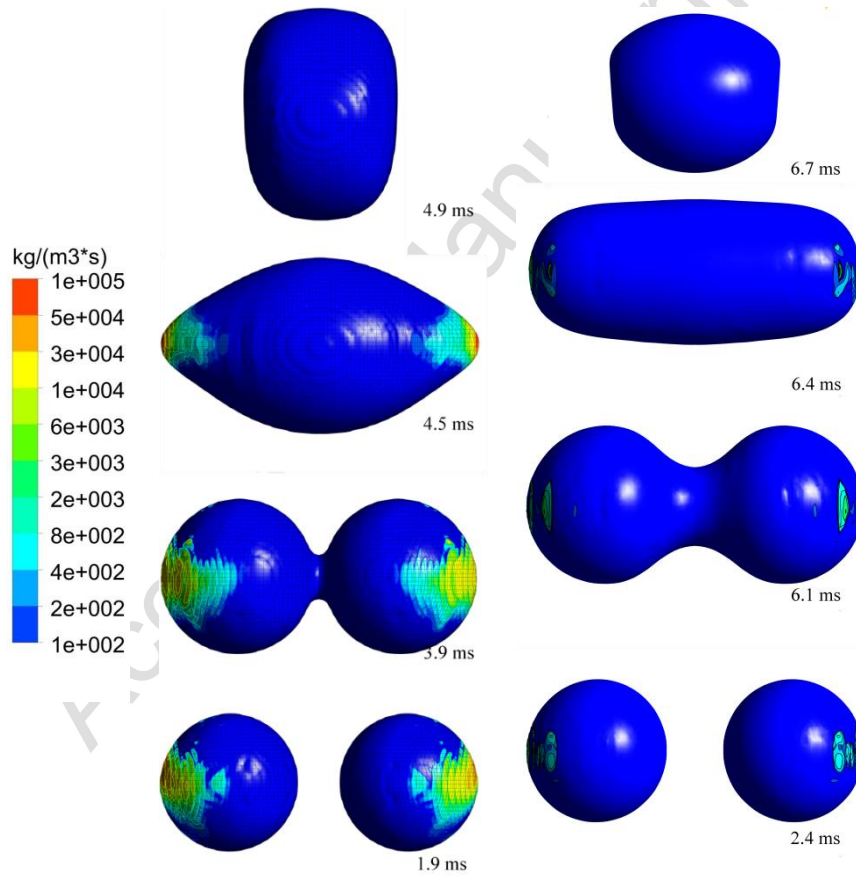

Figure 13. Evaporation rate contour at different times. Constant wall heat flux $q = 28 \frac{kW}{m^2}$ (Left), and $14 \frac{kW}{m^2}$ (Right), with inlet Re =549, and saturation temperature $Tsat = 300.15\ K$.
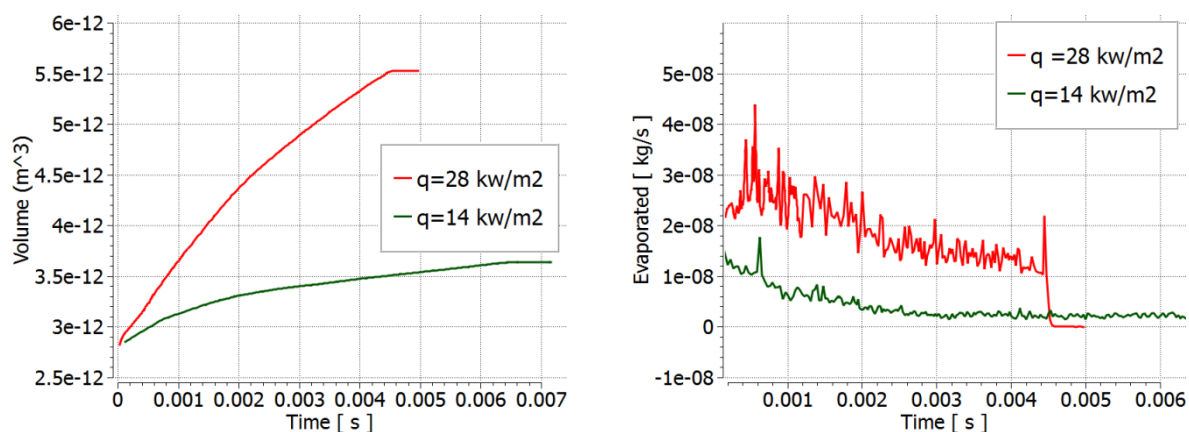
20

Figure 14. Bubble growth and total evaporation rate at different times. Constant wall heat flux $q = \ 14 \ and \ 28 \frac{kW}{m^2}$, inlet Reynolds number Re =549, and saturation temperature is $Tsat = 300.15 \ K$.

21

Table 1 Simulation parameters

Operating parameters	Case 1	Case 2	Case 3	Case 4
Reynolds number	7,8	7,8	7,8	7,8
Capillary number	0,004	0,014	0,031	0,069

Table 2 Properties of the working fluid

	Density (kg/m^3)	Eo	Mo	Surface Tension N/m	Viscosity Pa*s	Bubble Diameter mm	D to inlet mm	C to C Distance mm
Liquid	1273	16	0.0002	0.078	0.059	0.01	0.015	0.015
Gas	12.73				0.00059			

22